A deep learning approach to the texture optimization problem for friction control in lubricated contacts

Alexandre Silva[1,2], Veniero Lenzi[*1,2], Sergey Pyrlin[1,2], Sandra Carvalho[3], Albano Cavaleiro[3], Luís Marques[1,2]

[1] *Physics Center of Universities of Minho and Porto (CF-UM-UP), University of Minho, Campus de Gualtar, 4710-057, Braga, Portugal*

[2] *Laboratory of Physics for Materials and Emergent Technologies, LapMET, University of Minho, 4710-057 Braga, Portugal*

[3] *University of Coimbra, CEMMPRE - Centre for Mechanical Engineering Materials and Processes, Department of Mechanical Engineering, Rua Luís Reis Santos, 3030-788, Coimbra, Portugal*

* Corresponding author: Veniero Lenzi, E-mail: veniero.lenzi@fisica.uminho.pt

Abstract: The possibility to control friction through surface micro texturing could offer invaluable advantages in many fields, from wear and pollution reduction in the transportation industry to improved adhesion and grip. Unfortunately, the texture optimization problem is very hard to solve using traditional experimental and numerical methods, due to the complexity of the texture configuration space. In this work, we apply machine learning techniques to perform the texture optimization, by training a deep neural network to predict, with extremely high accuracy and speed, the Stribeck curve of a textured surface in lubricated contact. The deep neural network was used to completely resolve the mapping between textures and Stribeck curves, enabling a simple method to solve the texture optimization problem. This work demonstrates the potential of machine learning techniques in texture optimization for friction control in lubricated contacts.

Keywords: friction, surface texturing, optimization, deep learning, lubricated contact

1 Introduction

Our world is overwhelmed by the environmental impact of human activity and there is an imperative need to reduce pollution and mitigate its effects to avoid an irreversible global warming. The transportation industry, one of the largest contributors to polluting emissions, wastes a significant part of fuel and energy in overcoming friction forces between moving parts in contact [1] , meaning that any solution to reduce friction would provide huge environmental and economic benefits. Because of this, research on friction reduction has always been at the forefront of tribology research and many possible solutions exist, such as the application of surface coatings [2] and the use of more performing and environmentally friendly lubricant formulations [3]. One of the most promising ways to control the friction between contacting surfaces is provided by surface texturing, a process that is increasingly more efficient due to significant processing advances [4] allowing for rapid generation of patterned surfaces. It is well known that a fine control of friction through surface texturing can be achieved in nature. For example, sharks are covered in a regular array of denticles which help to achieve drag reduction [5]. The same reduction has been seen in the skin of snakes and certain lizards that developed scales to reduce dry contact friction [6]. Specific nano-hierarchically structured patterns found in the feet of tree toads [7], [8] and geckos [9] have been shown to provide a strong boundary friction, granting them better grip on vertical surfaces. In engineering applications, many different kinds of nature-inspired patterns have also been tested for friction control [8].

However, the design of these textures is in general based on trial-and-error methods, meaning that the optimal texture for a specific application is extremely hard to find. From an experimental perspective, textured samples need to be fabricated and tested, thus optimizing a specific pattern would require an extensive sampling of the texture parameter space, resulting in time and resource costs that are prohibitive [10], [11]. The same problem occurs when using numerical approaches to evaluate the tribological performance of a system, where the Stribeck curve [12] is calculated by solving the Reynolds equation [13], [14], for multiple sliding speeds, coupled with a model for treating the contact friction [15]. Even if the simulation process is faster as a whole when compared to a single experiment, the calculations still require typically minutes to complete, meaning that our ability to sample the possible configuration space is incredibly limited [16]. Moreover, the relationship between patterns and resulting Stribeck curves is expected to be highly non-linear, based on current experimental and numerical understanding [4], [17]–[19]. A possible solution to the apparently insurmountable texture optimization problem might be offered by machine learning techniques. Machine learning (ML) encompasses a large range of algorithms and modeling tools used for large data processing tasks [20], [21] with typical applications being classification and regression problems in information technology [22], [23]. One of the most prominent ML techniques is represented by deep neural networks (DNN), which are used with considerable success in many fields of physics, from applications in condensed matter [24], [25] and materials science [25], [26] to the solution of complex nonlinear equations [27], [28].

Tribo-informatics has recently emerged as a new research area combining tribology with big data methods such as machine learning and artificial intelligence techniques [29]–[31]. These approaches can help in establishing new correlations in tribological data to predict the behavior of novel materials, provide novel insights and a broader understanding of the friction and wear mechanisms [32]. A recent example is the development by Almqvist of a physics-informed neural network (PINN) capable of solving the one-dimensional Reynolds equation [33]. This approach is meshless, thus it solves one of the main bottlenecks in traditional numerical solutions of lubricated contacts, that is the reliance on a mesh. What makes DNNs particularly appealing for the texture optimization problem is their universal approximation capability [22], [23], coupled with their extreme speed when compared to traditional methods [28]. In texture optimization problems, DNNs have been used to optimize the features of periodic patterns of nanopillars in optic metamaterials to achieve the desired properties, i.e., high electromagnetic wave absorption in some frequency windows [28]. In these works, a DNN replaced the Maxwell equations solver, and it could predict -in millisecond time- an absorbance spectrum based solely on the periodic pattern features.

In this work we developed an effective method for the optimization of surface texturing patterns for friction applications based on a deep neural network. The DNN was designed and trained to accurately predict the Stribeck curve of a dimple textured surface, thus replacing the standard Reynolds equation solver in the solution of the forward problem. Moreover, to solve the inverse problem, a fast search-based approach was implemented to predict a set of candidate surface parameters (dimple pattern and dimple radius) that yield a set of closely matching Stribeck curves. The performance and accuracy of the DNN and the inverse approach were validated by comparing with the solutions provided by a numerical solver of the Reynolds and contact friction model equations.

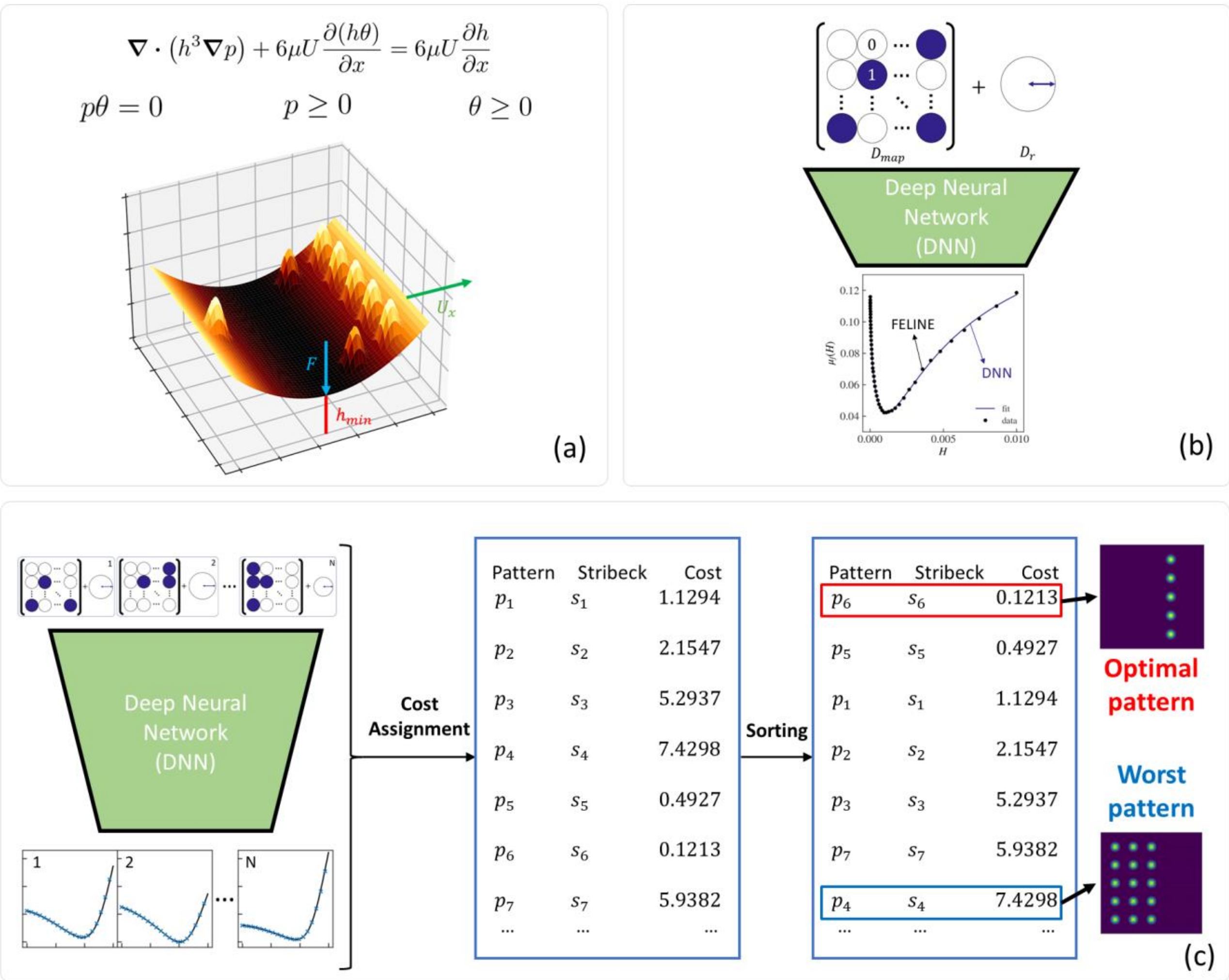

Figure 1. Schematic representation of the implementation of the DNN solution for the forward and inverse problem in texture optimization. (a) Non-conformal contact of surfaces subject to load F moving relative to each other with speed U, modeled as a height profile function $\mathbf{h}(\mathbf{x}, \mathbf{z})$. (b) Machine learning approach to predict the Stribeck curve of a textured surface, defined as the forward problem. The texture has 25 possible dimples (in a 5x5 grid with their presence represented in binary) and a fixed dimple radius for every dimple, therefore 26 parameters are capable of fully describing the texture. The output is a set of 7 parameters that allows for the reconstruction of the Stribeck curve. (c) Machine learning approach to solve the texture optimization problem (inverse problem). The Stribeck curves of the full configuration space are obtained by using the forward DNN. A cost value is then assigned to each pattern/Stribeck pair and a sorting algorithm is applied to obtain the extreme cases.

2 Methods

2.1 Model for lubricated non-conformal contact of textured surfaces

We consider a parabolic shape fully lubricated non-conformal contact of total area A similar to a lubricated journal bearing. Let $h_0 \equiv h_0(x, y)$ describe the untextured gap geometry (height profile) between the two surfaces moving in relative motion with speed U while subject to an external load F, as it is schematically represented in Fig. 1(a). The texturing is introduced by creating a 5x5 grid of cosine square shaped dimples. The dimple profile heights h_d are added to the untextured profile so that the textured gap geometry is defined as

$$h \equiv h_0(x, y) + h_d(x, y) \quad \textbf{(1)}$$

where h is the total height profile, h_0 is the untextured gap geometry height profile and h_d is the dimple textured gap geometry height profile (further details on the contact geometry can be found in SI, Section I).

To obtain the pressure profile p within the lubricant we solve the Reynolds equation, derived from the Navier-Stokes equations [14] after considering the lubricant film to be at constant temperature T, constant density ρ, and constant viscosity μ. Additionally, we do not consider any surface deformation effects, therefore the shape of the height profile remains constant throughout the simulations. The influence of the divergent domain on the film density is the possible formation of film rupture caused by cavitation (formation of vapor filled cavities) [34]–[37]. To consider this effect we introduce a system of equations for the pressure p and cavitation fraction θ profiles:

$$\nabla \cdot (h^3 \nabla p) + 6\mu U \frac{\partial (h\theta)}{\partial x} = 6\mu U \frac{\partial h}{\partial x} \tag{2}$$

$$p\theta = 0 \tag{3}$$

$$p \geq 0 \tag{4}$$

$$\theta \geq 0 \tag{5}$$

The system of Eqs. (1)-(4) represents a linear complementarity problem (LCP) [38]–[40], which was solved using the inexact Newton (INE) method [41] by restructuring the system of equations into a damped Newton iteration. The INE method ensures that the solution follows the non-negativity conditions at every iteration, thus providing a correct physical description of cavitation boundaries [16].

Depending on sliding speed, applied load and viscosity, the system admits three different regimes of lubricated contact: boundary, mixed and hydrodynamic, which differ in their main friction mechanisms. In this work only the mixed and hydrodynamic regimes have been considered since they occur in the presence of lubricant within the contact whereas in the boundary regime the surfaces are in direct contact (dry friction). To treat the mixed contact regime, both the hydrodynamic and asperity contact forces need to be considered in the same model. To this end, we decided to adopt a load-sharing approach [42], where the total friction force results from the combination of the hydrodynamic and contact terms:

$$f_t = f_{hydro} + f_{GT}. \tag{6}$$

The first term, valid only in regions where film rupture does not occur, represents the hydrodynamic component of friction, and depends on the pressure gradient generated within the lubricant film,

$$f_{hydro} = \left(\frac{h}{2}\frac{\partial p}{\partial x} + \frac{U\mu}{h}\right) A_f, \tag{7}$$

where A_f is the area of the full film domain. The second term of Eq. (5) represents the contact component of friction, that was calculated using the Greenwood-Tripp (GT) contact model [15, 42], which considers the roughness of both contacting surfaces. The GT contact model was chosen because it is simpler to implement while providing a qualitative treatment of friction [43]. Clearly, the GT contact model is not the best choice, as it is known to underestimate the pressure [44]–[46] and more accurate choices exist [47]. However, the focus of this work is to demonstrate the applicability of a DNN to solve the optimization problem of textured surfaces in lubricated contact, which does not depend on the particular choice of the solver used to generate training data.

In the GT model, the total load carried is defined as

$$f_{GT} = \tau_0 A_a + \mu_{asp} W_{asp}, \tag{7}$$

where τ_0 is the Eyring shear stress, A_a is the asperity contact area, W_{asp} is the load carried by asperities in the contacting surfaces, μ_{asp} is the coefficient of friction of the asperities [43], [48]. The load carried by asperities is defined as

$$W_{asp} = \frac{16\sqrt{2}}{5}\pi(\eta k \sigma)^2 \sqrt{\frac{\sigma}{k}} A E' F_{5/2}\left(\frac{h}{\sigma}\right). \tag{8}$$

The asperity contact area is similarly defined as

$$A_a = \pi^2 (\eta k \sigma)^2 A F_2 \left(\frac{h}{\sigma}\right), \tag{9}$$

The functions $F_{n/m}(h/\sigma)$ are statistical functions that account for the Gaussian distribution of asperities and can be approximated through a parametric fit [49]. The chosen values of the parameters $\eta, k,$ and σ present in Eqs. (8)-(9) reflect the typical values for a well-polished steel surface [15]. It should be noted that this roughness scale is much smaller than dimple characteristic dimensions. A table of numerical values for the parameters used in data generation in the training of the deep neural network is available in Section 3 of SI.

An open-source finite element implementation of the solver for the system of Eqs. (1)-(6), FELINE [50], was specifically developed and used to generate the training data and validate DNN results.

2.2 Method of solution and Stribeck curve calculation

To obtain the Stribeck curve, one must compute the coefficient of friction (COF) for each relevant sliding speed as the surface integral of the total friction force in (5), written as:

$$COF(H) = \frac{1}{WA}\int_{\Omega} f_t(H)\ d\Omega, \qquad \textbf{(10)}$$

where

$$H = \frac{\mu U}{F} \qquad \textbf{(11)}$$

is a dimensionless parameter dependent of the relative sliding speed termed Hersey number, and W is the total load carried, including both the hydrodynamic and contact term. A total of 50 different Hersey number values, equally spaced in a logarithmic scale, were used for each Stribeck curve in the interval $H \in [10^{-5}, 10^{-2}]$. This is equivalent to a procedure where the relative sliding speed is changed in the interval U $\in [0.043, 43]\ m/s$.

For every value of H, the COF is calculated when the total load carried balances the applied load F. For this purpose, we first perform a solver run with an initial condition for the minimum separation h_{min}. The total carried load W is then calculated and compared with F, andthe minimum separation h_{min} is adjusted by lowering (raising) it if W is smaller (larger) than F. After three iterations a spline interpolation is used to accelerate convergence, which is reached when $F^{-1}(W - F) < 10^{-3}$.

2.3 Design and training of the DNN

The textured surface in a lubricated contact is defined by a set of parameters: the dimple map D_{map} of dimension (D_x, D_y) which describes the presence and position of dimples on the surface (see Section 1 of S.I.), the dimple depth D_d, the dimple radius D_r, the parabolical edge E_0, and the surface roughness parameters $\eta k\sigma$. The value of dimple depth was fixed to $D_d^0 = 6\ \mu m$ to isolate the influence of dimple radius. This way, the complexity of the optimization problem is greatly reduced, with only one tunable parameter present in addition to the dimple map. Further details regarding the effect of D_r and D_d on load carrying capacity (LCC) and h_{min} of textured contacts can be found in SI.

Due to the fact that we considered a 5×5 grid of dimples with 6 possible D_r values in the interval $[40, 60]\ \mu m$, our network input consists of 26 parameters, that is 25 possible spots for dimple placement represented as Boolean variables and a globally applied value for dimple radius. The D_r interval was selected since it provides a sufficient range for optimization while remaining within the validity conditions of the Reynolds equation. Even if such configuration space appears simple at a first glance, it contains a total of $N = 6 \times 2^{25} \approx 2.01 \times 10^8$ possible texture configurations, rendering the texture optimization problem impossible to solve for any traditional solution approach.

In order to represent all Stribeck curves in the configuration space with the same number of parameters, we performed a fit of our data calculated with FELINE using a rational polynomial form defined as

$$f_n^m(x) = \frac{p_1 x^n + p_2 x^{n-1} + \cdots + p_n x + p_{n-1}}{x^m + q_1 x^{m-1} + \cdots + q_{m-1} x + q_m}, \qquad \textbf{(12)}$$

with polynomial degrees $(n, m) = (3, 3)$. This rational polynomial was found to be the best compromise between accuracy and total number of parameters when representing a Stribeck curve.

As a result, the DNN output consists of 7 rational fit parameters that allow the reconstruction of the Stribeck curve, thus reducing the overall number of output parameters while not significantly affecting precision. This fitting step regularizes the output of the network.

Regarding the DNN architecture, we adopted a simple topology consisting of 6 fully connected hidden layers with a number of neurons {32, 64, 96, 96, 64, 32} under no regularization using the ReLU activation function with He normal initialization [51] due to its performance and simplicity [52], [53].Since the number of hidden layers in our network is small and the width of these layers is sufficiently large, we do not expect the "dying ReLU problem" in this study [54] . The optimizer of choice was Nadam as it incorporates Nesterov momentum (with default hyperparameters) and can improve the convergence of the learning process [55]–[57]. To further optimize the training process, we sampled the validation set loss as a function of learning rate after 10 steps of training. This allowed us to carefully select a value for the learning rate (10^{-3}). The RMSE of the predicted rational fit coefficients was used as the network loss function. The training and testing process was implemented with Python 3.9 using the Keras high-level API [58] of TensorFlow version 2 [59].

The DNN training set was populated by randomly sampling sets of dimple maps $\boldsymbol{D_{map}}$, whose corresponding patterns were solved for all the D_r values to obtain the corresponding Stribeck curves. In total, around 60000 different combinations of patterns and dimple radii were computed using the FELINE solver, which required 6 days of computation time on 300 simultaneously running processes on Intel(R) Xeon(R) CPU E5-2697 v2 cores. This dataset was standardized according to the StandardScaler utility in the scikit-learn python package [60].

Owing to the fact that the boundary pressure is the same at $y = 0$ and $y = L$, we expect that a mirror reflection of any pattern over the $y = L/2$ axis does not change the corresponding Stribeck curve. This symmetry was explicitly included in the dataset by assigning the same Stribeck curve both to a pattern and to its reflection. This step is important in enhancing the overall physical accuracy of the DNN, while requiring no additional generation of data. From the generated dataset we selected 10% as a validation set, thus our resulting training set contains 54000 pairs of surface parameters and Stribeck curves and accounts for only 0.05% of the total configuration space.

3 Results and discussion

3.1 Solution of the forward problem

The forward problem, schematically represented in Fig. 1(b), was solved and examples of the DNN predictions are shown in Fig. 2 for a few cases in the validation set compared to data produced with the FELINE solver. The median RMSE of cases in the validation set is 5.7×10^{-4}, meaning that the network predictions are very accurate and show no appreciable difference with the Stribeck curves calculated with FELINE.

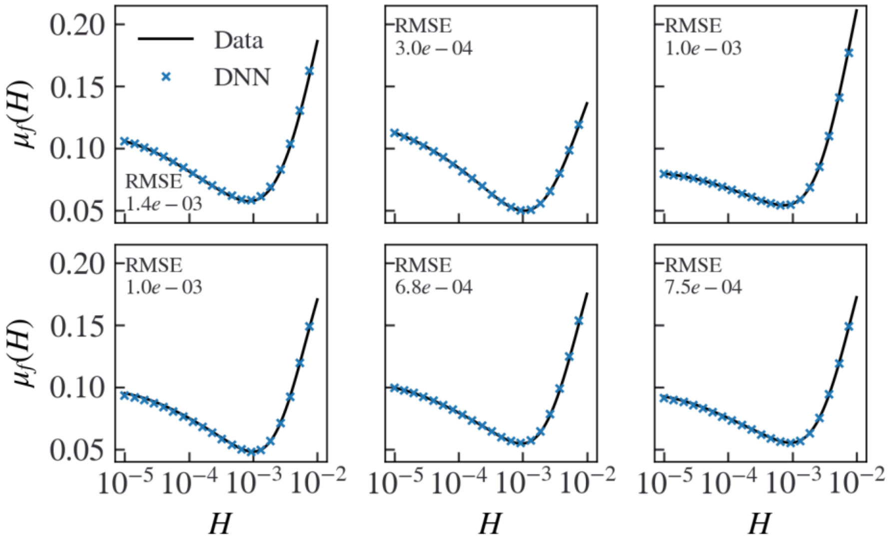

Figure 2. Network prediction of the Stribeck curves for randomly selected patterns in the validation set. The prediction accuracy is evaluated in terms of the root mean squared error (RMSE) in comparison to true data. The DNN results (crosses) have been down sampled for clarity.

Fig. 3(a) shows a histogram of the RMSE distribution for the validation set predictions of the full Stribeck curve and, for two separate regimes of the Stribeck curve, that is the mixed regime and the hydrodynamic regime. The same analysis was performed on a test set of patterns (~4000 samples) and it was verified that the network performs well on an arbitrary set of patterns (see SI, section X). To correctly establish boundaries for these regimes we used the lambda parameter criteria [61]:

$$\lambda = \frac{h_{min}}{\sigma}, \tag{83}$$

where h_{min} denotes the minimum thickness of the lubricant film (or minimum distance between the contacting films) and σ is one of the surface roughness parameters. For $\lambda > 3$ the contact regime is said to be hydrodynamic, while the mixed regime occurs for $1 < \lambda < 3$. After taking an average of λ for all curves in the validation set we found that the averaged value $H = 0.0015$ represents well the point in which the lubrication regime changes. Therefore, for $H \in [0, 0.0015]$ we have the mixed regime and for $H \in [0.0015, 0.01]$ we have the hydrodynamic regime.

The corresponding median, 95th and 99th percentile of the different histograms is reported in Table 1. Low RMSE values ($< 10^{-3}$) are consistently encountered in all regimes, indicating that the trained DNN is reliable across all the data. However, a better accuracy of the DNN in the mixed region was observed, compared to the hydrodynamic region. This is likely due to the larger span of COF values in the hydrodynamic region, for the same number of training samples, resulting in a lower accuracy prediction of the DNN therein.

Table 1 Median, 95th and 99th percentile of the RMSE values shown in the histogram in Fig. 3(b).

Regime	Median	99%	95%
Mixed	2.4×10^{-4}	7.9×10^{-4}	6.0×10^{-4}
Hydrodynamic	9.4×10^{-4}	6.1×10^{-3}	3.8×10^{-3}
Total	5.7×10^{-4}	3.4×10^{-3}	2.1×10^{-3}

To assess the quality of the trained network, it is also important to verify its ability to interpolate and extrapolate results in terms of the dimple radius, since it was trained only with 6 possibilities for it. In this regard, we compared both the network and the FELINE solver solutions for values in-between and outside the dimple radius interval 40 μm to 60 μm.

A pattern was randomly picked and its corresponding Stribeck curve was computed with the DNN and FELINE in order to obtain a RMSE of their difference, which was plotted in Fig. 3(c) as a function of D_r. As one can see in Fig. 3(c), in region (II), the interpolation region, there is a small difference between the interpolation results from the DNN and the corresponding ones from the FELINE solver, showing that the network is capable of accurate interpolating behavior.

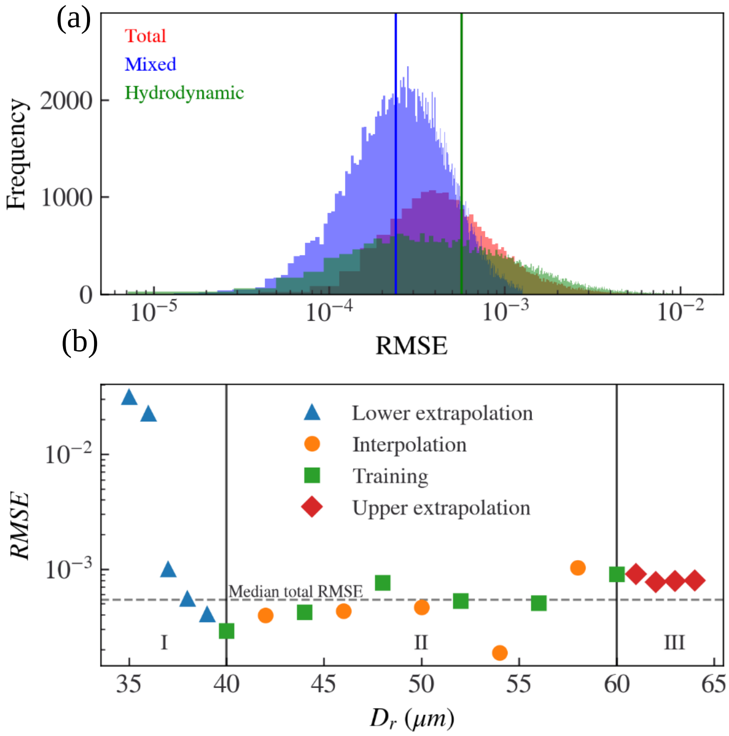

Figure 3. (a) Histogram of the RMSE for all patterns in the validation set in different regimes. The medians for the mixed, hydrodynamic, and total regions are also shown. (b) Interpolation and extrapolation study of dimple radius versus RMSE where: (I) indicates the lower extrapolation bound $D_r \in [35, 39]$, (II) the interpolated values $D_r \in [42, 46, 50, 54, 58]$ and the values used in training, (III) the upper extrapolation bound $D_r \in [61, 65]$.

For the extrapolation cases, regions (II) and (III), we see that the lower extrapolation bound works significantly worse than the upper extrapolation bound. In the hydrodynamic regime of lubrication, the COF increases linearly with increasing Hersey number. Contrary to this, in the mixed regime of lubrication, the COF increases exponentially with decreasing Hersey number. Extrapolation is typically more accurate for linear behavior, hence resulting in a larger extrapolation error for the lower bound of extrapolation.

In terms of timing, the DNN is 10^6 times faster when compared to the FELINE solver. In conclusion, we have successfully designed a DNN that meets the requirements of speed and accuracy needed to fully solve the texture optimization problem for tribological applications.

3.2 Solution of the inverse problem

The inverse problem, schematically represented in Fig. 1(c), consists in the ability to predict optimal patterns starting from desired characteristics of a particular system. With our capable forward problem DNN solver it is possible to obtain the Stribeck curve for every case in the full configuration space defined by 25 possible dimples and 6 possible radii, that is a total of about 3.3×10^8 cases. Let (p_k, s_k) stand for the k-th Pattern/Stribeck pair in the configuration space and consider a value, or cost, $C \equiv C(p_k, s_k)$ that we can assign to each pair, such as the minimum of the Stribeck curve s_k. By sorting the list of possible cases by their cost, we obtain the cases with smallest COF minimum and also highest COF minimum at the top and bottom of the list, respectively. The simple and straightforward algorithm Quicksort [62] was employed for this task.

The resulting optimal pattern for obtaining the smallest COF minimum using this method is shown in Fig. 4(a) and the corresponding Stribeck curve (solved with both FELINE and the DNN) is also reported in Fig. 4(b), compared with the untextured case. We observe that in this case the dimples are present only in a small region right after h_{min}. The pressure and cavitation profiles of the contact obtained using FELINE, for the predicted optimal texture at the lowest friction point in the Stribeck curve are reported in Fig. 5(a) and 5(b), respectively. We observed an increase in pressure in the convergent gap and also a smaller pressure increase in the divergent gap. Furthermore, a significant drop in the cavitation profile led to an overall reduction of the size of the cavitation region in the divergent gap. The presence of dimples right after the h_{min} zone appears to hinder the formation of the cavitation region. Thus, the optimal pattern results in smaller film rupture areas and larger pressures in the convergent area.

The configuration space sorting also allows us to find the pattern that yields the largest COF minimum. We found a family of very similar patterns that generated almost indistinguishable Stribeck curves, as shown in Fig. 4(c)-(d). In this case, the convergent region of the contact is fully textured, including the h_{min} area. By looking at the pressure profile (Fig. 5(c)) we observed a significant pressure drop in the convergent gap. This is caused by the presence of dimples in a region that produces most of the hydrostatic pressure that counters the applied load. Such dimple placement disrupts the pressure profile. The cavitation profile (Fig. 5(d)) also displayed a decrease in magnitude, but the total cavitation area was not affected by this.

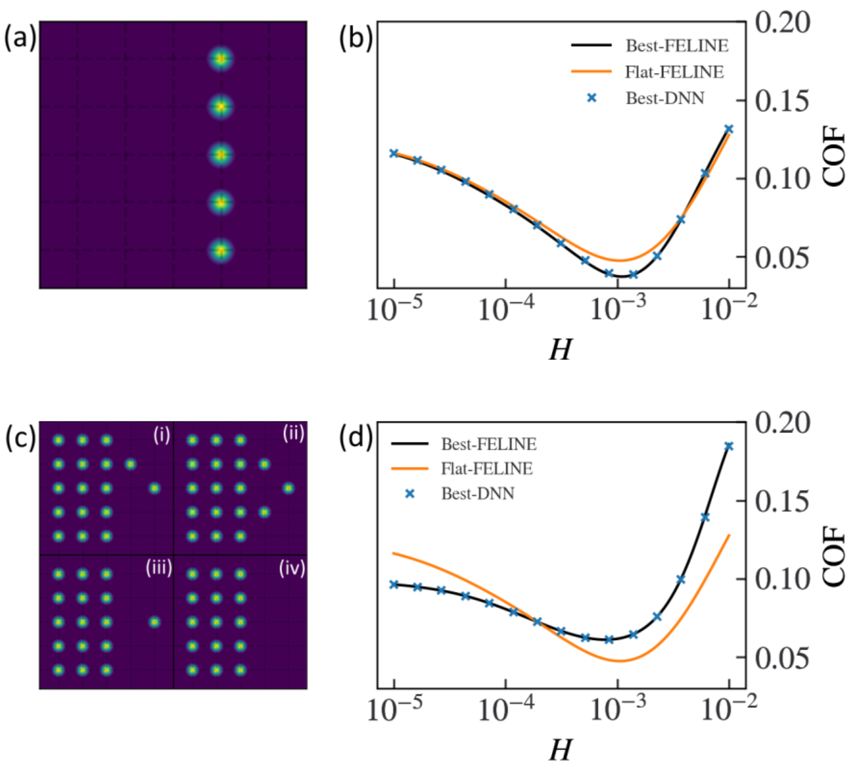

Figure 4. Resulting patterns and Stribeck curves from the cost assignment and sorting method used to find the optimal friction reducing/increasing patterns in the mixed regime. (a) Optimal pattern that yields the Stribeck curve with the smallest minimum. The corresponding Stribeck curve, calculated with both FELINE and the DNN, is reported in panel (b), where it is compared with the untextured case. (c) Family of textures that yield nearly matching Stribeck curves with the largest COF minimum. The Stribeck curve of pattern (i) calculated with both FELINE and the DNN is reported in panel (d), where it is compared with the untextured case. The DNN results (crosses) have been down sampled for clarity.

Curiously, the two families of patterns that provide a significant decrease (Fig. 4(a)) and increase (Fig. 4(c)) in COF, have been already observed and described by Tala and collaborators [63]. The reasoning behind the friction increase/decrease phenomena described in Tala et. al. accurately matches the observations of our own neural network predictions and further investigation done with FELINE. This fact demonstrates that our solution of the inverse problem is capable of correctly identifying the optimal texturing pattern. In terms of accuracy, the DNN solutions are basically indiscernible from the FELINE ones.

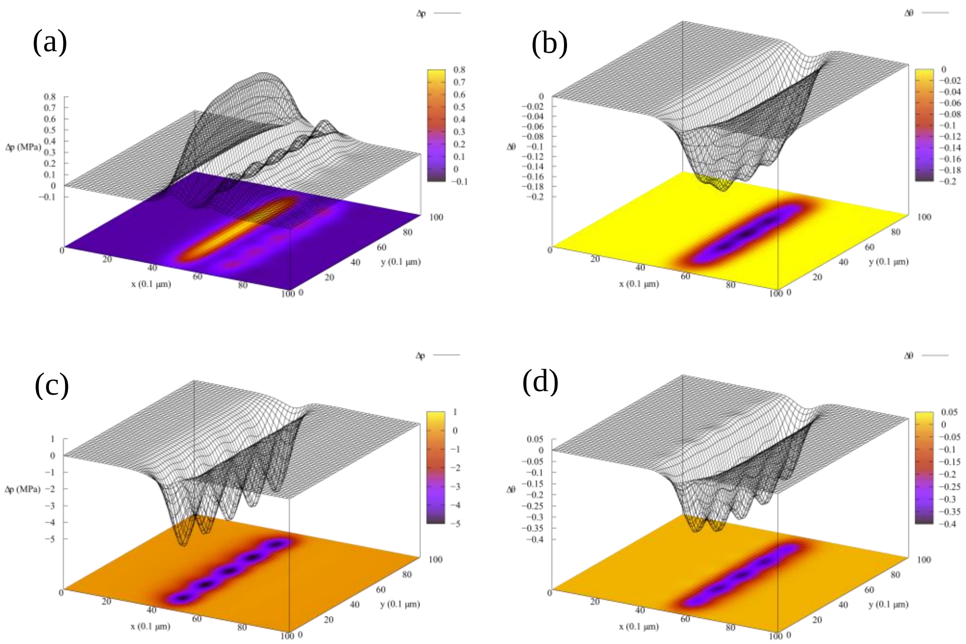

Figure 5. Pressure and cavitation profiles, determined at the Hersey number of the COF minimum of the untextured case Stribeck curve. For the optimal pattern in Fig. 4(a) for friction reduction and for friction gain in Fig. 4(c). (a) Pressure difference between the untextured and textured case in Fig. 4(a). (b) Cavitation difference between the untextured and textured case in Fig. 4(a). (c) Pressure difference between the untextured and textured case in Fig. 4(c). (d) Cavitation difference between the untextured and textured case in Fig. 4(c).

The collection of similar patterns (i)-(iv) shown in Fig. 4(c) exemplifies an important feature of a method like this, which is the ability to find nearly identical solutions generated by different patterns. This can be extremely important from an experimental point of view because, at parity of performance, a particular texture may be better in terms of manufacturing cost/speed in a laboratory.

To further test our inverse problem solver, we looked for a pattern that reduces friction in the hydrodynamic regime. To achieve this, we defined a more elaborate form of the cost:

$$C(p_k, s_k) = \int_{H_1}^{H_2} [s_k(H) - s_0(H)]\ dH, \qquad \textbf{(9)}$$

where H_1, H_2 encompass the hydrodynamic range. This function computes the area under the Stribeck curve in the hydrodynamic region for some Stribeck curve $s_k \in L$ minus the area under the Stribeck curve of the untextured case, s_0. The lowest value of C should correspond with the pattern that maximizes the reduction of the COF in the hydrodynamic regime.

The resulting optimal pattern for maximizing the reduction of the COF in the hydrodynamic regime using this method is shown in Fig. 6(a), and the corresponding Stribeck curve (solved with both FELINE and the DNN) is also reported in Fig. 6(b), compared with the untextured case. The corresponding pressure and cavitation profile differences with the untextured cases are reported in Fig. 7(a) and 7(b), respectively. It is possible to observe an increase of pressure in the convergent and divergent gaps (Fig. 7(a)). Concerning cavitation, only a slight reduction of the size of the cavitation region in the divergent gap was observed.

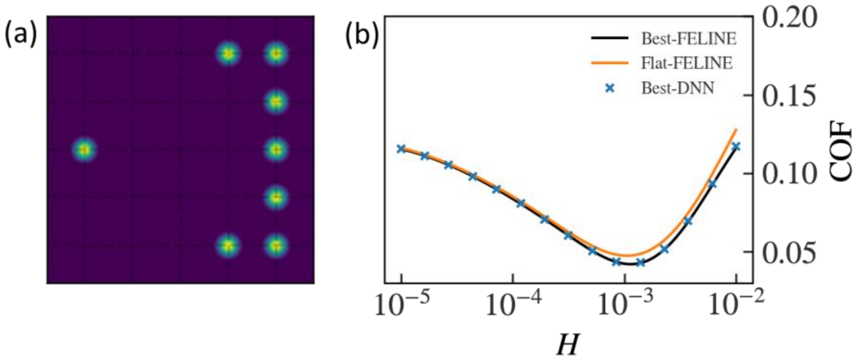

Figure 6. Resulting pattern and Stribeck curves from the cost assignment and sorting method used to find the optimal friction reducing pattern in the hydrodynamic regime. (a) Optimal pattern that yields the Stribeck curve with the overall smallest COF in the hydrodynamic regime. The corresponding Stribeck curve, calculated with both FELINE and the DNN is reported in panel (b), where it is compared with the untextured case. The DNN result (crosses) has been down sampled for clarity.

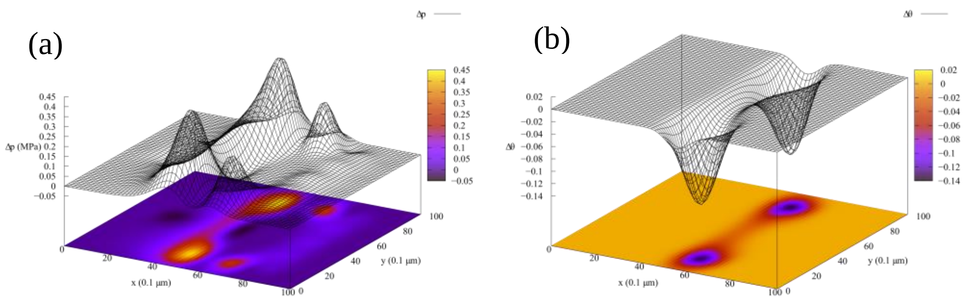

Figure 7. Pressure and cavitation profiles, determined at the Hersey number of the COF minimum of the untextured case Stribeck curve. For the optimal pattern in Fig. 7(a) for friction reduction. (a) Pressure difference between the untextured and textured case in Fig. 7(b). (b) Cavitation difference between the untextured and textured case in Fig. 7(b).

The absolute values of h_{min} and the percent deviations of the difference of h_{min} relative to the untextured case for the optimal texture cases for friction reduction/gain are represented, respectively, in Fig. 8(a) and 8(b). For the optimal texture for friction reduction in the mixed regime (orange line in Fig. 8), a ~12% increase in the h_{min} in the mixed regime and a ~10% decrease of h_{min} at larger H numbers was observed. Additionally, for the mixed regime, calculations also show a ~5% increase in the LCC coupled with a ~22% decrease in the overall cavitation region area, resulting in a smaller COF for these sliding speeds. For the optimal texture for friction gain (cyan line in Fig. 8), an 80-90% decrease in h_{min} in the mixed regime was observed, stabilizing around a 60% decrease at larger H numbers. Concerning LCC and cavitation area, a 33% decrease and no change in the overall cavitation region were found, explaining the significant increase in COF for this pattern. Finally, for the optimal texture for friction reduction in all regimes (green line in Fig. 8), a ~5% increase in h_{min} in the mixed regime was observed, while no appreciable variation could be seen at larger H numbers. A ~3% increase in the LCC, coupled with a ~16% decrease in overall cavitation region area, shows a similar performance compared to the Fig. 4(a) pattern. The combination of these effects results in a slight decrease of COF for nearly all sliding speeds. Textures that are capable of an effective reduction of friction and increase in LCC can highly contribute to extend the service life of the lubricated contact

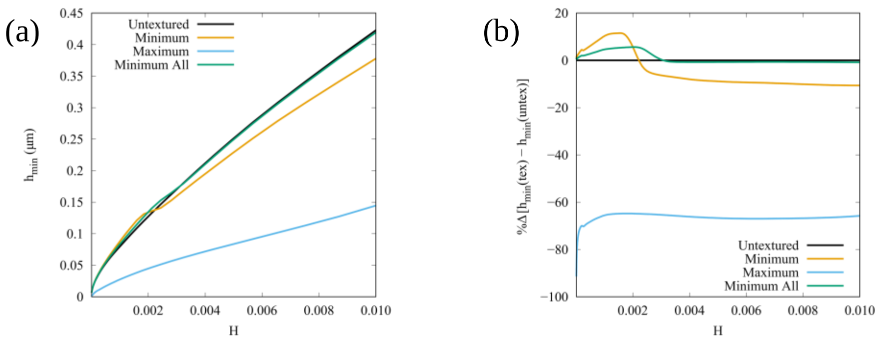

Figure 8. Effect of texturing on the minimum film thickness as a function of the Hersey number. (a) Comparison between the untextured case and the three cases determined by the neural network, where Minimum is the texture of Fig. 4(a), Maximum is the texture of Fig. 4(c)(i) and Minimum All is the texture of Fig. 6(a). (b) Percentual deviation of the difference of h_{min} with respect to the untextured case.

The above optimal textures, and in particular the ones in Fig. 4(a) and Fig. 4(c), clearly demonstrate the capability of our approach for texture optimization problems. In fact, the solution of the inverse problem for the lowest and highest COF values returned the expected optimal textures [63]. The strength of this method is that the proposed solutions are actually the best ones, since all of the possible configuration space has been explored. This demonstrates how the texture optimization problem turns in to a very simple task using a DNN to solve forward problem, which allowed for a very efficient solution of texture configuration space.

4 Conclusions

We have successfully designed and trained a deep neural network capable of accurately predicting the resulting Stribeck curve generated by a dimpled texture with median root mean square errors of 5.7×10^{-4}. This type of texture, composed of an array of 5×5 possible dimples with dimple radius D_r has an unpredictable and highly non-linear effect on the surface friction coefficient. The DNN can efficiently compute all possible cases of a total of around 300 million possibilities, trained with only 0.05% of them, thus enabling us to solve the texture optimization problem which is otherwise impossible to treat by traditional experimental and numerical methods. We determined both extremes of an optimization problem by taking advantage of the incredible performance of our DNN, predicting the relevant optimal textures in the process. We investigated properties of the developed DNN such as accuracy, extrapolation, and interpolation capabilities, demonstrating its robustness and reliability. This work paves the way for the use of deep learning as a tool to realize careful friction control of surfaces through optimally designed textures.

Acknowledgements

This work was supported by the Portuguese Foundation for Science and Technology (FCT, I.P.) in the framework of the Strategic Funding UIDB/04650/2020, projects PTDC/EME-SIS/30446/2017, project

POCI-01–0247-FEDER-045940, and Advanced Computing Project CPCA/A2/4513/2020 for accessing MACC-BOB HPC resources.

Declaration of competing interest

The authors have no competing interests to declare that are relevant to the content of this article.

Electronic Supplementary Material (ESM)

Electronic Supplementary Material: Supplementary material (add a brief description) is available in the online version of this article).

Data availability statement

All the data used in this work is available free of charge from **https://doi.org/10.34622/datarepositorium/MUVOJD**

References

[1] K. Holmberg, P. Andersson, and A. Erdemir, “Global energy consumption due to friction in passenger cars,” *Tribol. Int.*, vol. 47, pp. 221–234, Mar. 2012, doi: 10.1016/j.triboint.2011.11.022.

[2] “A review of recent progress in coatings, surface modifications and alloy developments for solid oxide fuel cell ferritic stainless steel interconnects - ScienceDirect.” https://www.sciencedirect.com/science/article/abs/pii/S0378775309017285?via%3Dihub (accessed Feb. 16, 2023).

[3] “Lubricants | Free Full-Text | A Review of Ionic Liquid Lubricants.” https://www.mdpi.com/2075-4442/1/1/3 (accessed Feb. 16, 2023).

[4] “State of the Art in Laser Surface Texturing | J. Tribol. | ASME Digital Collection.” https://asmedigitalcollection.asme.org/tribology/article-abstract/127/1/248/462965/State-of-the-Art-in-Laser-Surface-Texturing?redirectedFrom=fulltext (accessed Feb. 16, 2023).

[5] “A brief review of bio-inspired surface technology and application toward underwater drag reduction - ScienceDirect.” https://www.sciencedirect.com/science/article/abs/pii/S0029801820300457?via%3Dihub (accessed Feb. 16, 2023).

[6] “Bio-inspired scale-like surface textures and their tribological properties - IOPscience.” https://iopscience.iop.org/article/10.1088/1748-3190/10/4/044001 (accessed Feb. 16, 2023).

[7] T. Endlein *et al.*, “Sticking like sticky tape: tree frogs use friction forces to enhance attachment on overhanging surfaces,” *J. R. Soc. Interface*, vol. 10, no. 80, p. 20120838, Mar. 2013, doi: 10.1098/rsif.2012.0838.

[8] “Micro–Nano Hierarchical Structure Enhanced Strong Wet Friction Surface Inspired by Tree Frogs - Zhang - 2020 - Advanced Science - Wiley Online Library.” https://onlinelibrary.wiley.com/doi/10.1002/advs.202001125 (accessed Feb. 16, 2023).

[9] A. Y. Stark, I. Badge, N. A. Wucinich, T. W. Sullivan, P. H. Niewiarowski, and A. Dhinojwala, “Surface wettability plays a significant role in gecko adhesion underwater,” *Proc. Natl. Acad. Sci.*, vol. 110, no. 16, pp. 6340–6345, Apr. 2013, doi: 10.1073/pnas.1219317110.

[10] M. Marian, A. Almqvist, A. Rosenkranz, and M. Fillon, “Numerical micro-texture optimization for lubricated contacts—A critical discussion,” *Friction*, vol. 10, no. 11, pp. 1772–1809, Nov. 2022, doi: 10.1007/s40544-022-0609-6.

[11] “Tribology of polymers: Adhesion, friction, wear, and mass-transfer - ScienceDirect.” https://www.sciencedirect.com/science/article/pii/S0301679X05001891 (accessed Feb. 16, 2023).

[12] R. Stribeck, “Kugellager für beliebige Belastungen,” *Z. Vereines Dtsch. Ingenieure*, vol. 45, pp. 73–79, Feb. 2023.

[13] “On a Model for the Prediction of the Friction Coefficient in Mixed Lubrication Based on a Load-Sharing Concept with Measured Surface Roughness | SpringerLink.” https://link.springer.com/article/10.1007/s11249-015-0536-z (accessed Feb. 16, 2023).

[14] “IV. On the theory of lubrication and its application to Mr. Beauchamp tower’s experiments, including an experimental determination of the viscosity of olive oil | Philosophical Transactions of the Royal Society of London.” https://royalsocietypublishing.org/doi/10.1098/rstl.1886.0005 (accessed Feb. 16, 2023).

[15] “The Contact of Two Nominally Flat Rough Surfaces - J. A. Greenwood, J. H. Tripp, 1970.” https://journals.sagepub.com/doi/10.1243/PIME_PROC_1970_185_069_02 (accessed Feb. 16, 2023).

[16] D. Gropper, L. Wang, and T. J. Harvey, “Hydrodynamic lubrication of textured surfaces: A review of modeling techniques and key findings,” *Tribol. Int.*, vol. 94, pp. 509–529, Feb. 2016, doi: 10.1016/j.triboint.2015.10.009.

[17] C. Greiner, T. Merz, D. Braun, A. Codrignani, and F. Magagnato, “Optimum dimple diameter for friction reduction with laser surface texturing: the effect of velocity gradient,” *Surf. Topogr. Metrol. Prop.*, vol. 3, no. 4, p. 044001, Sep. 2015, doi: 10.1088/2051-672X/3/4/044001.

[18] R. Ausas, P. Ragot, J. Leiva, M. Jai, G. Bayada, and G. C. Buscaglia, “The Impact of the Cavitation Model in the Analysis of Microtextured Lubricated Journal Bearings,” *J. Tribol.*, vol. 129, no. 4, pp. 868–875, Apr. 2007, doi: 10.1115/1.2768088.

[19] R. F. Ausas, M. Jai, and G. C. Buscaglia, “A Mass-Conserving Algorithm for Dynamical Lubrication Problems With Cavitation,” *J. Tribol.*, vol. 131, no. 3, Jun. 2009, doi: 10.1115/1.3142903.

[20] “Rev. Mod. Phys. 91, 045002 (2019) - Machine learning and the physical sciences.” https://journals.aps.org/rmp/abstract/10.1103/RevModPhys.91.045002 (accessed Feb. 16, 2023).

[21] M. Biehl and A. Mietzner, “Statistical Mechanics of Unsupervised Learning,” *Europhys. Lett.*, vol. 24, no. 5, p. 421, Nov. 1993, doi: 10.1209/0295-5075/24/5/017.

[22] K. Hornik, M. Stinchcombe, and H. White, “Multilayer feedforward networks are universal approximators,” *Neural Netw.*, vol. 2, no. 5, pp. 359–366, Jan. 1989, doi: 10.1016/0893-6080(89)90020-8.

[23] “Approximation by superpositions of a sigmoidal function | SpringerLink.” https://link.springer.com/article/10.1007/BF02551274 (accessed Feb. 16, 2023).

[24] J. Carrasquilla and R. G. Melko, “Machine learning phases of matter,” *Nat. Phys.*, vol. 13, no. 5, Art. no. 5, May 2017, doi: 10.1038/nphys4035.

[25] “Deep learning model to predict fracture mechanisms of graphene | npj 2D Materials and Applications.” https://www.nature.com/articles/s41699-021-00228-x (accessed Feb. 16, 2023).

[26] “Artificial intelligence and machine learning in design of mechanical materials - Materials Horizons (RSC Publishing).” https://pubs.rsc.org/en/content/articlelanding/2021/MH/D0MH01451F (accessed Feb. 16, 2023).

[27] “Phys. Rev. Lett. 120, 024102 (2018) - Model-Free Prediction of Large Spatiotemporally Chaotic Systems from Data: A Reservoir Computing Approach.” https://journals.aps.org/prl/abstract/10.1103/PhysRevLett.120.024102 (accessed Feb. 16, 2023).

[28] “Deep learning for accelerated all-dielectric metasurface design.” https://opg.optica.org/oe/fulltext.cfm?uri=oe-27-20-27523&id=418820 (accessed Feb. 16, 2023).

[29] “Frontiers | Artificial Neural Networks (ANNs) as a Novel Modeling Technique in Tribology.” https://www.frontiersin.org/articles/10.3389/fmech.2019.00030/full (accessed Feb. 16, 2023).

[30] M. Marian and S. Tremmel, “Current Trends and Applications of Machine Learning in Tribology—A Review,” *Lubricants*, vol. 9, no. 9, Art. no. 9, Sep. 2021, doi: 10.3390/lubricants9090086.

[31] “Tribo-informatics: Concept, architecture, and case study | SpringerLink.” https://link.springer.com/article/10.1007/s40544-020-0457-3 (accessed Feb. 16, 2023).

[32] “A review of recent advances in tribology | SpringerLink.” https://link.springer.com/article/10.1007/s40544-020-0367-2 (accessed Feb. 16, 2023).

[33] “Lubricants | Free Full-Text | Fundamentals of Physics-Informed Neural Networks Applied to Solve the Reynolds Boundary Value Problem.” https://www.mdpi.com/2075-4442/9/8/82 (accessed Feb. 16, 2023).

[34] E. H. G and A. M. L, “A computer program for cavitation and starvation problems.,” *Leeds Lyon Symp Tribol.*, vol. 1st, pp. 37–41, 1975.

[35] *The finite journal bearing, considering vaporization: (Das Gleitlager von endlicher Breite mit Verdampfung).* 1957.
[36] “Modelling Cavitation in (Elasto)Hydrodynamic Lubrication | IntechOpen.” https://www.intechopen.com/chapters/51347 (accessed Feb. 16, 2023).
[37] M. Giacopini, M. T. Fowell, D. Dini, and A. Strozzi, “A Mass-Conserving Complementarity Formulation to Study Lubricant Films in the Presence of Cavitation,” *J. Tribol.*, vol. 132, no. 4, Sep. 2010, doi: 10.1115/1.4002215.
[38] R. W. Cottle, J.-S. Pang, and R. E. Stone, *The Linear Complementarity Problem*. Society for Industrial and Applied Mathematics, 2009. doi: 10.1137/1.9780898719000.
[39] “A New Approach for Studying Cavitation in Lubrication | J. Tribol. | ASME Digital Collection.” https://asmedigitalcollection.asme.org/tribology/article-abstract/136/1/011706/376505/A-New-Approach-for-Studying-Cavitation-in?redirectedFrom=fulltext (accessed Feb. 16, 2023).
[40] “Fluid film lubrication in the presence of cavitation: a mass-conserving two-dimensional formulation for compressible, piezoviscous and non-Newtonian fluids - ScienceDirect.” https://www.sciencedirect.com/science/article/abs/pii/S0301679X13002211 (accessed Feb. 16, 2023).
[41] “An inexact Newton method for solving complementarity problems in hydrodynamic lubrication | SpringerLink.” https://link.springer.com/article/10.1007/s10092-018-0244-9 (accessed Feb. 16, 2023).
[42] K. L. Johnson, J. A. Greenwood, and S. Y. Poon, “A simple theory of asperity contact in elastohydro-dynamic lubrication,” *Wear*, vol. 19, no. 1, pp. 91–108, Jan. 1972, doi: 10.1016/0043-1648(72)90445-0.
[43] R. I. Taylor, “Rough Surface Contact Modelling—A Review,” *Lubricants*, vol. 10, no. 5, Art. no. 5, May 2022, doi: 10.3390/lubricants10050098.
[44] M. H. Müser *et al.*, “Meeting the Contact-Mechanics Challenge,” *Tribol. Lett.*, vol. 65, no. 4, p. 118, Aug. 2017, doi: 10.1007/s11249-017-0900-2.
[45] W. B. Dapp, A. Lücke, B. N. J. Persson, and M. H. Müser, “Self-Affine Elastic Contacts: Percolation and Leakage,” *Phys. Rev. Lett.*, vol. 108, no. 24, p. 244301, Jun. 2012, doi: 10.1103/PhysRevLett.108.244301.
[46] J. A. Greenwood and J. J. Wu, “Surface Roughness and Contact: An Apology”.
[47] “Phys. Rev. B 74, 075420 (2006) - Practical Green’s function approach to the simulation of elastic semi-infinite solids.” https://journals.aps.org/prb/abstract/10.1103/PhysRevB.74.075420 (accessed Feb. 16, 2023).
[48] “Fundamentals of Fluid Film Lubrication | Bernard J. Hamrock, Steven R.” https://www.taylorfrancis.com/books/mono/10.1201/9780203021187/fundamentals-fluid-film-lubrication-bo-jacobson-steven-schmid-bernard-hamrock (accessed Feb. 16, 2023).
[49] “Fundamentals of Tribology.” https://www.worldscientific.com/worldscibooks/10.1142/p553#t=aboutBook (accessed Feb. 16, 2023).
[50] “FELINE: Finite element solver for hydrodynamic lubrication problems using the inexact Newton method - ScienceDirect.” https://www.sciencedirect.com/science/article/pii/S001046552200159X?via%3Dihub (accessed Feb. 16, 2023).
[51] K. He, X. Zhang, S. Ren, and J. Sun, “Delving Deep into Rectifiers: Surpassing Human-Level Performance on ImageNet Classification.” arXiv, Feb. 06, 2015. doi: 10.48550/arXiv.1502.01852.
[52] “Hardware and Software Optimizations for Accelerating Deep Neural Networks: Survey of Current Trends, Challenges, and the Road Ahead | IEEE Journals & Magazine | IEEE Xplore.” https://ieeexplore.ieee.org/document/9269334 (accessed Feb. 16, 2023).
[53] A. F. Agarap, “Deep Learning using Rectified Linear Units (ReLU).” arXiv, Feb. 07, 2019. doi: 10.48550/arXiv.1803.08375.
[54] L. Lu, Y. Shin, Y. Su, and G. E. Karniadakis, “Dying ReLU and Initialization: Theory and Numerical Examples,” *Commun. Comput. Phys.*, vol. 28, no. 5, pp. 1671–1706, Jun. 2020, doi: 10.4208/cicp.OA-2020-0165.
[55] S. J. Reddi, S. Kale, and S. Kumar, “On the Convergence of Adam and Beyond.” arXiv, Apr. 19, 2019. doi: 10.48550/arXiv.1904.09237.
[56] S. Salman and X. Liu, “Overfitting Mechanism and Avoidance in Deep Neural Networks.” arXiv, Jan. 19, 2019. doi: 10.48550/arXiv.1901.06566.
[57] “Vanishing Gradient Mitigation with Deep Learning Neural Network Optimization | IEEE Conference Publication | IEEE Xplore.” https://ieeexplore.ieee.org/document/8843652 (accessed Feb. 16, 2023).
[58] “Keras: Deep Learning for humans.” Keras, Feb. 16, 2023. Accessed: Feb. 16, 2023. [Online]. Available: https://github.com/keras-team/keras
[59] M. Abadi *et al.*, “TensorFlow: Large-Scale Machine Learning on Heterogeneous Distributed Systems.” arXiv, Mar. 16, 2016. doi: 10.48550/arXiv.1603.04467.
[60] F. Pedregosa *et al.*, “Scikit-learn: Machine Learning in Python,” *Mach. Learn. PYTHON*.

[61] “Lubricant film formation in rough surface non-conformal conjunctions subjected to GPa pressures and high slide-to-roll ratios | Scientific Reports.” https://www.nature.com/articles/s41598-020-77434-y (accessed Feb. 16, 2023).
[62] “Algorithm 64: Quicksort | Communications of the ACM.” https://dl.acm.org/doi/10.1145/366622.366644 (accessed Feb. 16, 2023).
[63] N. Tala-Ighil, M. Fillon, and P. Maspeyrot, “Effect of textured area on the performances of a hydrodynamic journal bearing,” *Tribol. Int.*, vol. 44, no. 3, pp. 211–219, Mar. 2011, doi: 10.1016/j.triboint.2010.10.003.